

Nanoconcentration of Terahertz Radiation in Plasmonic Waveguides

Anastasia Rusina,¹ Maxim Durach,¹ Keith A. Nelson,² and Mark I. Stockman^{1,3}

¹*Department of Physics and Astronomy, Georgia State University, Atlanta, Georgia 30303, USA*

²*Department of Chemistry, MIT, Cambridge, MA 02139, USA*

³*On sabbatical leave at Ecole Supérieure de Physique et de Chimie Industrielle de la Ville de Paris, 10, rue Vauquelin, 75231 Paris, CEDEX 05, France*

(Dated: November 1, 2021)

Recent years have seen an explosive research and development of nanoplasmonics in the visible and near-infrared (near-ir) frequency regions.¹ One of the most fundamental effects in nanoplasmonics is nano-concentration of optical energy. Plasmonic nanofocusing has been predicted² and experimentally achieved.^{3,4,5} Nanoconcentration of optical energy at nanoplasmonic probes made possible optical ultramicroscopy with nanometer-scale resolution^{6,7,8} and ultrasensitive Raman spectroscopy.⁹ It will be very beneficial for the fundamental science, engineering, environmental, and defense applications to be able to nano-concentrate terahertz radiation (frequency 1 – 10 THz or vacuum wavelength $\lambda_0 = 300 - 30 \mu\text{m}$). This will allow for the nanoscale spatial resolution for THz imaging¹⁰ and introduce the THz spectroscopy on the nanoscale, taking full advantage of the rich THz spectra and submicron to nanoscale structures of many engineering, physical, and biological objects of wide interest: electronic components (integrated circuits, etc.), bacteria, their spores, viruses, macromolecules, carbon clusters and nanotubes, etc. In this Letter we establish the principal limits for the nanoconcentration of the THz radiation in metal/dielectric waveguides and determine their optimum shapes required for this nanoconcentration. We predict that the adiabatic compression of THz radiation from the initial spot size of $R_0 \sim \lambda_0$ to the final size of $R = 100 - 250 \text{ nm}$ can be achieved with the THz radiation intensity increased by a factor of $\times 10$ to $\times 250$. This THz energy nanoconcentration will not only improve the spatial resolution and increase the signal/noise ratio for the THz imaging and spectroscopy, but in combination with the recently developed sources of powerful THz pulses¹¹ will allow the observation of nonlinear THz effects and a carrying out a variety of nonlinear spectroscopies (such as two-dimensional spectroscopy), which are highly informative. This will find a wide spectrum of applications in science, engineering, biomedical research, environmental monitoring, and defense.

There are existing approaches to deep subwavelength THz imaging and probing based on sharp tips irradiated by a THz source,¹² adiabatically-tapered metal-dielectric waveguides¹³ similar to optical adiabatic concentrators,^{2,3,4,5} and nonlinear microscopic THz sources.¹⁴ For the development of the THz nanotechnology, it is extremely important to understand spatial limits to which the THz radiation energy can be concentrated (nanofocused).

A major challenge for the nanoconcentration of the electromagnetic energy in the THz region is the large radiation wavelength in vacuum or conventional dielectrics, $\lambda_0 = 30 \mu\text{m} - 300 \mu\text{m}$, where the THz radiation can only be focused to the relatively very large regions of size $\sim \lambda_0/2$. The developed field of optical energy concentration, which is based on surface plasmon polaritons (SPPs), suggests that one of the ways to solving this problem is to employ the surface electromagnetic waves (SEWs). In the far infrared (ir), the dielectric permittivity of metals has large imaginary part which dominates over its negative real part.¹⁵ This implies that SEWs propagating along a metal-dielectric flat interface in this frequency range, known as Sommerfeld-Zenneck waves,^{16,17} are weakly bound to the surface¹⁸ and can hardly be used for the confinement of THz radiation.

It has been suggested that periodically perforating flat surfaces of ideal metals with grooves or holes leads to the appearance of SEWs, which mimic (“spoof”) SPPs to be

stronger bound to the surfaces^{19,20,21} permitting a better control over the THz fields. It has been predicted that SPPs on an array of parallel grooves cut on the surface of a perfect conductor wire can be localized by adiabatic deepening of the grooves.²² At a point, where grooves are approximately a quarter of wavelength of light, the highest concentration is achieved to be on the order of tens of micrometers. This method restricts the localization point to a particular frequency, making the concentration very narrow-band. Also, the depth of a groove should be $\approx \lambda_0/4$, i.e., in the tens to hundred micron range, which precludes completely nanoscale devices.

It is well known from microwave technology that the ideal-metal waveguides with smooth surfaces support TEM waves, where the electric field lines are either infinitely extended or terminate at the metal surfaces normally to them. The latter case requires the waveguide cross-section topology to be more than single-connected; an example may be a coaxial waveguide (“coax”). Such waveguides possess are very wide-band in frequency. The THz waveguides can be adiabatically tapered to concentrate energy. The idea of adiabatic energy concentration comes from ultramicroscopy^{23,24,25} and nanoplasmonics,² where it has been developed both theoretically and experimentally^{3,4,5} and used in ultrasensitive surface enhanced Raman spectroscopy.⁹ Employing these ideas of the adiabatic concentration and using a tapered metal-dielectric waveguide, the THz spatial resolution achieved

is $\sim 20 \mu\text{m}$ across the entire THz spectrum.¹³

In this Letter, for the first time, we establish the fundamental limits and find the principles of designing the optimum and efficient metal/dielectric waveguides suitable for the THz nanofocusing. The specific examples are for the wide-band concentrators: a plasmonic metal wedge cavity and tapered coax waveguides, which are terminated by funnel-type adiabatic tapers. Such nano-concentrators along with the advent of high-power sources^{11,26} and sensitive detectors²⁷ of THz radiation, will open up an extremely wide range of possible THz applications, in particular, in material diagnostics, probe nanoimaging, biomedical applications etc. – cf. Refs. 28,29,30.

Note that an alternative approach to the THz energy concentration using doped semiconductor tapers has also been proposed.³¹ However, the required heavy doping of the semiconductors may cause fast electron relaxation due to the collisions with the inflicted lattice defects and bring about high losses. Therefore, in this Letter we will pursue the adiabatic nanoconcentration of the THz radiation using metal/dielectric structures.

Conventionally for THz and microwave regions, the metals are considered as ideal which is equivalent to neglecting their skin depth $l_s = \lambda_0 / \text{Re} \sqrt{-\varepsilon_m}$, where ε_m is the permittivity of the metal (we take into account that in the THz region $|\varepsilon_m| \gg 1$), and $\lambda_0 = c/\omega$ is the reduced wavelength in vacuum. It is true that in the THz region $l_s = 30 - 60 \text{ nm}$. i.e., $l_s \ll \lambda_0$. However, as we show below in this Letter, it is the finite skin depth, though as small as it is, that principally limits the ultimate localization size of the THz fields. For larger waveguides, the THz wave energy is localized mostly in the vacuum (dielectric) and its losses, which occur in the metal's skin layer, are correspondingly small. The effective quality factor (or, figure of merit) of the waveguide, which shows how many periods the wave can propagate without significantly losing its energy, can be estimated as

$$Q \sim 2a/l_s, \quad (1)$$

where a is the characteristic minimum size of the waveguide; this estimate becomes a good approximation for a metal-dielectric-metal planar waveguide [see below Eq. (2)]. When the waveguide size reduces to become on the order of the skin depth, $a \lesssim l_s$, the THz field is pushed into the metal, and the quality factor reduces to $Q \lesssim 1$, which implies strong losses. Qualitatively, this establishes the limit to the nanoconcentration: for upper THz region $a \gtrsim l_s \approx 30 \text{ nm}$, while for the 1 THz frequency $a \gtrsim l_s \approx 60 \text{ nm}$. These are the practical limits of the THz nanoconcentration for the noble metals (silver, gold, and platinum) and for aluminum.

If one pursues the goal of creating enhanced local fields in a small region, but not necessarily to efficiently transfer the THz energy from the far field to the near field, then the apertureless SNOM approach, where a sharp metal or dielectric tip is irradiated by THz radiation, can, in principle, achieve even higher resolution.³² However,

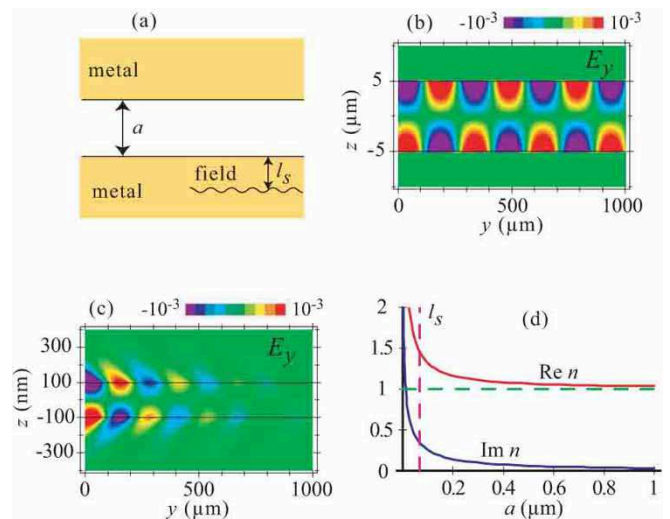


FIG. 1: Geometry and properties of the THz TM mode in a parallel metal-slab waveguide. (a) Schematic of the waveguide. The width of the dielectric gap a and the skin depth l_s are indicated. (b) An instantaneous distribution of the longitudinal electric field E_y along the propagation coordinate y for $a = 10 \mu\text{m}$ and frequency 1 THz in a silver-vacuum-silver waveguide. (c) The same as in panel (b) but for $a = 200 \text{ nm}$. (d) Modal refractive index $n = k/k_0$ ($\text{Re } n$ is denoted by the red line and $\text{Im } n$ by the blue line) as a function of the waveguide width a . Dashed green line indicates the value of n for the perfect conductor. Skin-depth value is shown by the vertical dashed line.

the efficiency of utilizing the THz energy of the source in this case will be extremely low; the stray, far-field THz energy may create a significant parasitic background.

Here and below in this Letter, we consider examples of the THz adiabatic nanoconcentration quantitatively, where the effect of the specific geometry will become apparent. Consider first a parallel plate waveguide that consists of a dielectric slab of thickness a with dielectric permittivity ε_d sandwiched between two thick metal plates (with thickness of at least a few l_s , i.e., greater than 200 nm in practical terms) [see Fig.1(a)]. The permittivity of the metal ε_m in the THz region has a very large ($\gtrsim 10^6$) imaginary part that defines the very small skin depth $l_s \lesssim 100 \text{ nm}$, which justifies the usual consideration of the metals as perfect conductors.¹⁵ However, as we have already mentioned, for our purposes of the THz nanoconcentration, we need to take into account the field penetration into the metal, which makes the problem plasmonic. In this case, the propagating modes of the system are SPPs, which are TM modes characterized by the symmetry with respect to the reflection in the center plane. We will orient the coordinate system with its z axis normal to the plane and the y axis in the direction of propagation. The symmetric (even) modes have even field components H_x and E_z and odd E_y ; the parity of the antisymmetric (odd) modes is opposite.

From plasmonics it is known that the even modes have a larger fraction of their energy localized in the dielec-

tric and the odd modes in the metal. Therefore, the even modes have much smaller damping and are, therefore, most suitable for the THz energy concentrations. The dispersion relation for the even modes is given in the Methods section as Eq. (5). This equation can be much simplified and solved in a closed analytical form taking into account that we are interested in the sub-wavelength focusing, i.e., $a \lesssim \lambda$, where $\lambda = \lambda_0/\varepsilon_d$ is the reduced wavelength in the dielectric; also, in the entire THz region $l_s \ll \lambda$. This shows that there exists a small parameter in the problem $l_s a/\lambda^2 \ll 1$ [see also Eq. (6)], which allows one to solve analytically the dispersion relation (5) obtaining the modal refraction index $n = k/k_0$, where k is the THz wavevector, and $k_0 = 1/\lambda_0$,

$$n = \sqrt{\varepsilon_d} \left(1 + \frac{l_s(1+i)}{a} \right)^{1/2} \approx \sqrt{\varepsilon_d} \left(1 + i \frac{l_s}{2a} \right), \quad (2)$$

where the approximate equality is valid for not too tight nanofocusing, i.e., for $l_s \ll a$. From this, we can obtain the quality factor of the waveguide $Q = \text{Re}n/\text{Im}n = 2a/l_s$, giving a quantitative meaning to the estimate (1).

Plasmonic effects (i.e. those of the finite skin depth) are illustrated in Fig. 1 for silver-vacuum-silver waveguide and frequency of 1 THz. Panels (b) and (c) display the longitudinal electric field E_y obtained by the exact solution of the Maxwell equations. Note that this field component is absent for the ideal conductor; here it is relatively small: on the order of 10^{-3} of the transverse field. Panel (b) illustrates the case of a relatively wide waveguide ($a = 10 \mu\text{m}$), where it is evident that the electric field is localized mostly in the dielectric region of the waveguide, and the extinction of the wave is small. In a sharp contrast, for a nanoscopic waveguide ($a = 200 \text{ nm}$) in panel (c), the electric field significantly penetrates the metal. In accord with our arguments, there is a very significant extinction of the fields as they propagate; the retardation effects are also evident: the lines of equal amplitude are at an angle relative to the normal (z) direction. The dependence of the modal refraction index on the thickness a of the waveguide obtained from Eq. (2) is plotted in Fig. 1 (d). This index increases as a becomes comparable with the skin depth. While $\text{Re}n$ and $\text{Im}n$ increase by the same absolute amount, the quality factor Q , obviously, greatly decreases with decrease of a . The mode described above can be used for broadband energy concentration of THz waves.

To introduce the THz nanoconcentration, consider a metal-dielectric-metal waveguide that is slowly (adiabatically) tapered off as a wedge, as illustrated in Fig. 2 (a). Because of the adiabatic change of the parameters, a wave propagating in such a waveguide will adjust to it without reflection or scattering, just as it takes place in nanoplasmonic waveguides.² As a result, propagating it will concentrate its energy, conforming to the tapering of the waveguide. The corresponding solution can be obtained from the Maxwell equations using the Wentzel-Kramers-Brillouin (WKB) approximation, similarly to the nanoplasmonic case in the visible,² as described in

the Methods section. The WKB approximation is applicable under the conditions that

$$\delta = |d(\text{Re}k^{-1})/dy| \ll 1, \quad |da/dy| \ll 1, \quad (3)$$

where δ is the well-known adiabatic parameter describing how slowly the modal wavelength changes on a distance of its own, and $|da/dy|$ is a parameter describing how adiabatically the transverse size of the confined mode changes along the propagation coordinate.

In the WKB approximation, the behavior of the dominating transverse field component E_z as a function of the coordinate y along the propagation direction is shown for the last $6 \mu\text{m}$ of the propagation toward the edge in Fig. 2 (b). There is a clearly seen spatial concentration of the energy and increase of the field as the wave is guided into the taper. The predicted behavior of the two components of electric field and the magnetic field for the last micron of the propagation is shown in panels (c)-(e). It apparently indicates the adiabatic concentration, without an appreciable loss of the intensity. The THz wave follows the waveguide up to the nanometric size.

The red line in Fig. 2 (f) indicates that the local intensity I as the function of the thickness a of the waveguide for $a < 4 \mu\text{m}$ increases significantly with $1/a$, in qualitative accord with the behavior expected for the negligibly low losses. This intensity reaches its maximum for $a = 1.6 \mu\text{m}$ and then starts to decrease as the losses overcome the adiabatic concentration. At smaller thicknesses, $a \lesssim 400 \text{ nm}$, the intensity in Fig. 2 (f) starts to increase again, which is unphysical. The reason is revealed by the behavior of the adiabatic parameter δ shown by the blue line: for $a \lesssim 400 \text{ nm}$, δ becomes relatively large (comparable with 1), i.e., the adiabaticity is violated. This is due to the fact that the fraction of the THz field energy propagating in the metal is dramatically increased for $a \lesssim 400 \text{ nm}$ due to the constricted transverse extension of the dielectric in the waveguide. This causes a significant loss per wavelength λ , leading to a rapid change of the wave vector k , breaking down the adiabaticity. This constitutes a fundamental difference from the nanoplasmonic adiabatic concentration in the optical region where the adiabatic parameter is constant, and the adiabaticity holds everywhere including the vicinity of the tip.²

To provide for the optimum guiding of the THz wave and its concentration on the nanoscale, the terminating (nanoscopic) part of the waveguide should be tapered slower, in a funnel-like manner. That is, one needs to decrease the grading da/dy of the waveguide near the edge in order to keep the adiabaticity parameter $\delta = |d(\text{Re}k^{-1})/da \times da/dy|$ approximately constant and small enough to prevent the back-reflection. Because for the adiabatic grading (tapering), the derivative $d(\text{Re}k^{-1})/da$ does not depend on the grading (it is the same as for the plane waveguide) and is only a function of a , the equation $\delta = \delta(y)$ is a differential equation for the shape of the waveguide that can be easily integrated. This results in the dependence of the thickness a on the

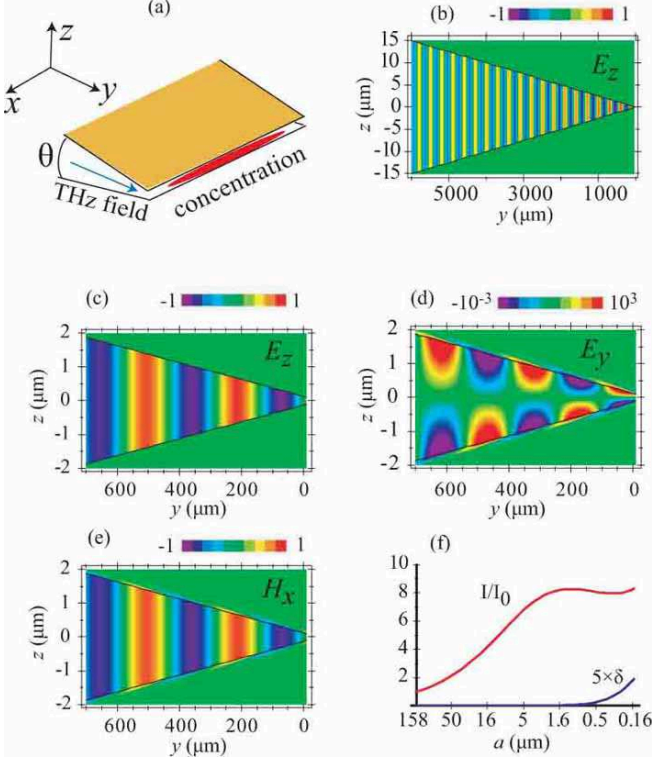


FIG. 2: Adiabatic concentration of THz field energy in a graded waveguide, where a dielectric wedge is surrounded by the thick silver layer. (a) Schematic of energy concentration, where θ is the wedge opening angle, the arrow indicates the direction of propagation of the THz wave, and the red highlights the area of the adiabatic concentration. The orientation of the coordinate system is shown in the inset. (b) An instantaneous distribution of the transverse electric field E_z of the THz wave propagating and concentrating along the wedge waveguide for the last 6 mm of the propagation toward the edge. Note the difference in scales in the z and y directions. (c) An instantaneous spatial distribution of the transverse electric field E_z close to the edge of the wedge, for the last 640 μm of the propagation. (d) The same as (c) but for the longitudinal (with respect to the propagation direction) component of the field E_y . (e) The same as (c) but for the transverse component of the magnetic field H_x . The units of these field components are arbitrary but consistent between the panels. (f) Dependence of THz field intensity in the middle of waveguide on the dielectric gap width a (the red line). The blue curve displays the dependence on a of the adiabatic parameter δ , scaled by a factor of 5. The values of a indicated at the successive horizontal axis ticks differ by a factor of $10^{-1/2}$, i.e., by 5 dB.

longitudinal coordinate y determined by a simple integral

$$\text{Re } n^{-1}(a) = k_0 \int \delta(y) dy, \quad (4)$$

where $n(a)$ is the modal index defined in this case by Eq. (2), and $\delta(y)$ is the desired dependence of the adiabatic parameter along the waveguide, which is an arbitrary function of y satisfying the adiabaticity conditions (3).

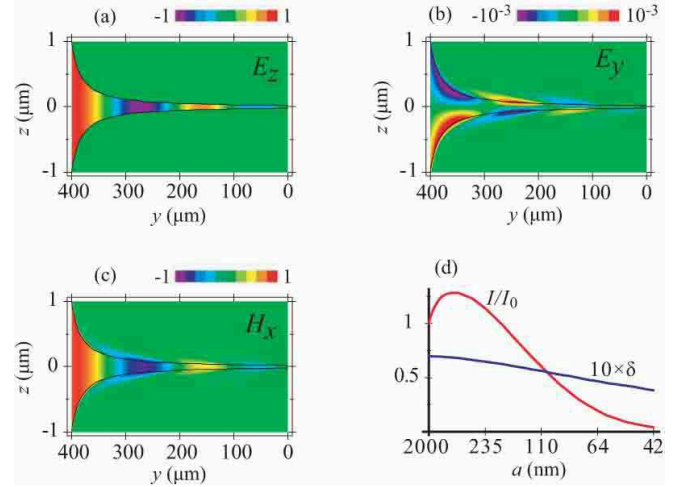


FIG. 3: Terahertz energy concentration in adiabatically tapered curved-wedge waveguide. (a) Instantaneous distribution of the transverse component of the THz electric field E_z (in the central plane $z = 0$) as a function of the coordinate y along the propagation direction for the last 400 μm of the propagation. (b) The same as in panel (a) but for the longitudinal electric field component E_y . (c) The same as panel (a) but for the transverse magnetic field H_x . The units for the fields are arbitrary but consistent between the panels. (d) The THz field intensity I (relative to the intensity I_0 at the entrance of the waveguide) as a function of the dielectric gap thickness a is shown by the red line. The adiabatic parameter scaled by a factor of 10 as a function of a is indicated by the blue line. The values of a indicated at the horizontal axis ticks correspond to the values of y at the ticks of panels (a)-(c).

The geometry of an adiabatically-tapered end of the silver/vacuum waveguide found from Eq. (4) and satisfying Eq. (3) and the corresponding WKB solutions for the 1 THz fields are shown in Fig. 3 (a)-(c). The optimum shape of the waveguide in this case is funnel-like, greatly elongated toward the edge. The nanoconcentration of the field is evident on panels (a)-(c), as well as its penetration into the metal for $a \lesssim 100$ nm. As these panels show quantitatively and the red curve on panel (d) qualitatively, the field intensity reaches its maximum at $a \approx 300$ nm where it is enhanced with respect to the field at the entrance to the funnel waveguide by a modest factor of 1.2. At the same time, the adiabatic parameter δ decreases toward the tip from 0.07 to 0.05, indicated the applicability of the WKB approximation everywhere. Note that the this funnel-shaped wedge, indeed, continues the linearly-graded wedge waveguide shown in Fig. 2, which yields the enhancement factor of ≈ 8 at $a = 2 \mu\text{m}$. Sequentially, these two waveguides provide the intensity enhancement by approximately $\times 10$ while compressing the THz wave to the thickness of $a = 300$ nm and the enhancement by a factor of 3 for $a = 100$ nm.

Thus, true nanolocalization of THz radiation in one dimension (1d) is possible. The minimum transverse size of this nanolocalization is determined by the skin depth,

as we have already discussed qualitatively in the introductory part of this Letter. The obtained 1d beam of the nanoconcentrated THz radiation may be used for different purposes, in particular as a source for the diffraction elements including the nanofocusing zone plates of the type introduced in Ref. 33.

The two-dimensional (2d) concentration of the THz radiation can be achieved by using an adiabatically-tapered conical coax waveguide, whose geometry is illustrated in Fig. 4 (a). The central metal wire of radius r is surrounded by a dielectric gap of the radial thickness a , which is enclosed by a thick (~ 200 nm or thicker) outer metal shell. Both r and a are smooth functions of the longitudinal coordinate y , which describes the tapering of the coax toward the apex (tip) at $y = 0$. The THz waves propagate from the wide end of the coax toward the apex, adiabatically following the tapering. In the spirit of WKB, for any particular y the wave behavior for the tapered coax is the same as for a cylindrical coax with the values of r and a equal to the local values $r(y)$ and $a(y)$.

The dispersion relation for the coax waveguide that takes into account the plasmonic effects (i.e., the penetration of radiation into the metal and the concurrent losses) is obtained in the Methods section as Eq. (9). Calculated from this expression, the dependence of the modal refractive index $n = k(a, r)/k_0$ on the dielectric gap a is displayed in Fig. 4 (b) for the frequency of 1 THz, silver as a metal, and vacuum in the dielectric gap. The results are shown for two values of the radius of the central wire: $r = 10 \mu\text{m}$ and $r = 60$ nm. As one can see, the real part of the modal index practically does not depend on r ; it starts growing when a decreases. The imaginary part of the index n increases when the central wire thickness r decreases, but this dependence is very weak. Both $\text{Re } n$ and $\text{Im } n$ grow dramatically for $r \lesssim l_s$. This is due to the penetration of the THz field into the metal, i.e., it is a plasmonic effect.

The WKB solution for the radial field E_ρ in the cross section of this coax waveguide is shown for the last $3 \mu\text{m}$ of the propagation toward the tip in Fig. 4 (c). The adiabatic following and energy concentration are evident in this panel. The penetration into the metal of the tangential (to the metal surface) field components E_y and H_φ is noticeable in Figs. 4 (d) and (e). The intensity I of the THz field (relative to the intensity I_0 at the entrance of the waveguide) as a function of the waveguide outer radius $R = r + a$ is shown by the red line in Fig. 4 (f). Dramatically, it shows the adiabatic nanoconcentration and the intensity increase by more than two orders of magnitude for the nanoconcentration from the waveguide radius $R = 300 \mu\text{m}$, where the THz radiation can be focused, toward $R = 300$ nm. However, the dramatic increase of the adiabatic parameter δ [plotted by the blue line in Fig. 4 (f)] for $R \lesssim 1 \mu\text{m}$ shows that these results can only be trusted for $R \gtrsim 1 \mu\text{m}$.

For the true 2d nanoconcentration of the THz radiation below this micron-scale radius, similar to the 1d case

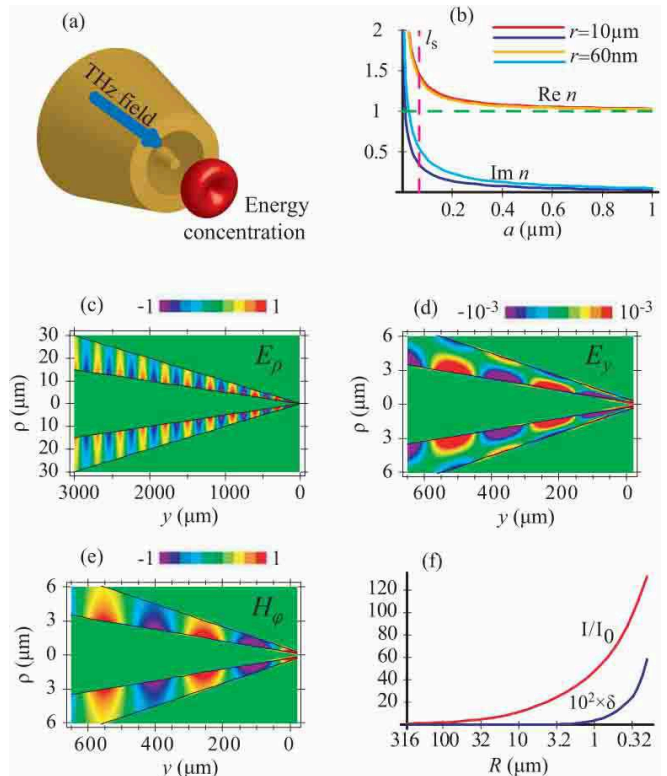


FIG. 4: Geometry, modal index of refraction, and THz energy concentration in conically-tapered metal-dielectric waveguide. (a) Schematic of geometry and energy concentration. The central wire and the coax shell are shown along with the schematic of the THz energy concentration. (b) Dependence of modal refractive index n in coaxial waveguide on the dielectric gap width a for two central wire radii: $r = 10 \mu\text{m}$ and $r = 60$ nm. The color coding of the lines is indicated. The dielectric in the gap is vacuum. (c) Instantaneous distribution of the radial THz electric field amplitude E_ρ in the cross section of the coax for the last $3 \mu\text{m}$ of the propagation toward the tip. The amplitude of the field is color coded by the bar at the top of the panel. (d) Instantaneous distribution of the longitudinal THz electric field amplitude E_y on the coordinate y for the last $620 \mu\text{m}$ of the propagation. (e) The same as (d) but for the transverse magnetic field H_φ . The units of these field components are arbitrary but consistent between the panels. (f) Dependence of THz field intensity in the middle of waveguide gap on the waveguide outer radius $R = r + a$ is shown in red. The blue curve displays the adiabatic parameter δ as a function of R , scaled by a factor of 10^2 . The values of R indicated at the successive horizontal axis ticks differ by a factor of $10^{-1/2}$, i.e., by 5 dB.

of the wedge, to preserve the adiabaticity, a funnel-like tapering is necessary. Generally, the tapering of the central wire and that of the outer metal shell do not need to be the same. However, we found that better results are obtained when it is the case, i.e., the waveguide is tapered-off self-similarly. In specific calculations, as everywhere in this Letter, we assume that the metal of the waveguide is silver, the dielectric is vacuum, and the frequency is 1 THz. Doing so, we have found the cor-

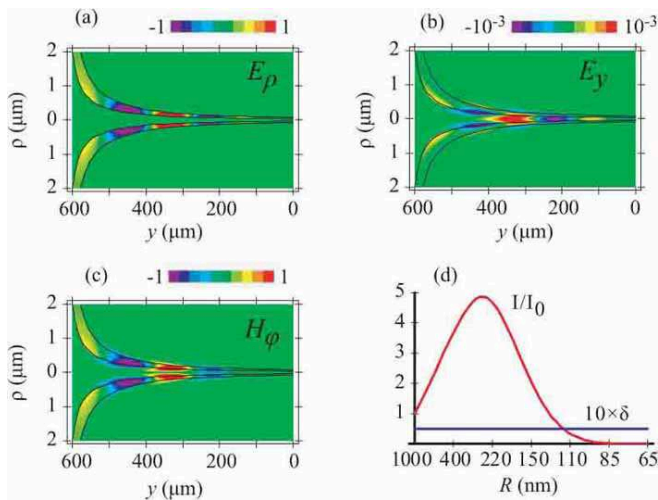


FIG. 5: Adiabatic terahertz energy concentration in a self-similarly curved, funnel-shaped coaxial waveguide, where the metal is silver, and the dielectric in the gap is vacuum. The dielectric gap is between the pair of the neighboring curved lines, and the metal is everywhere else. (a) Instantaneous distribution of the radial (transverse) component E_ρ of the electric field of the guided THz wave as a function of the propagation coordinate along the wedge y for the last $600 \mu\text{m}$ of the propagation. (b) The same for the longitudinal electric field component E_y . (c) The same for transverse magnetic field H_ϕ , whose lines form circles around the central metal wire. The units of these field components are arbitrary but consistent between the panels. (d) The THz intensity I as a function of the waveguide radius R , displayed relative to the intensity I_0 at the beginning of the waveguide (red line). Adiabatic parameter δ multiplied by a factor of 10 as a function of R (blue line). The values of the radius R shown at the ticks correspond to those of y shown in panels (a)-(c).

responding grading of the waveguide using Eq. (4) and setting $\delta = 0.05$, which is small enough to satisfy the adiabaticity very well. In this case, indeed, we have used the corresponding dispersion relation (9). The obtained shape of the waveguide is a strongly-elongated funnel, as shown in Fig. 5 (a)-(c). These figures display the THz fields that we have calculated in the WKB approximation for this waveguide. As one can see from these figures, within the last half micron of the propagation, the electric and magnetic fields of the THz wave efficiently follow the adiabatically curved waveguide. The penetration into the metal of the tangential (to the metal-dielectric interfaces) field components for $y < 400 \mu\text{m}$ is evident in panels (b) and (c). The longitudinal electric field component E_y is significantly localized in the central metal wire [panel(b)], which is a plasmonic effect.

The dependence of the THz field intensity in the gap (relative to the intensity I_0 at the entrance of this funnel) on the total radius of the waveguide R is shown in Fig. 5 (d) by the red line. In this case, the adiabatic concentration is very efficient. The intensity of the THz radiation increases by a factor of $\times 5$ when it is compressed from the initial radius of $R = 1 \mu\text{m}$ to the radius

$R \approx 250 \text{ nm}$. The penetration of the fields into the metal for smaller values of the radius R (tighter confinement) causes losses that dominate over the effect of the concentration. Again, we remind that this funnel waveguide is a continuation and termination for the straight cone that yields the field enhancement by $\times 50$ for $R = 1 \mu\text{m}$ [see Fig. 4 (f)]. Consecutively, these two waveguides (the initial cone continued and terminated by the funnel) are very efficient, adiabatically compressing the THz radiation from the initial radius $R = 300 \mu\text{m}$ to the radius $R = 250 \text{ nm}$ increasing its intensity by a factor $\times 250$. Even for the final radius $R = 100 \text{ nm}$, the total THz intensity is increased by a factor of $\times 10$ (which is the products of factors $\times 50$ for the cone part and $\times 0.2$ for the funnel). Thus, the optimally graded plasmonic-metal 2d waveguide is very efficient in the concentration and guidance of the THz fields with the transverse radius of confinement $R \lesssim 100 \text{ nm}$.

To discuss the results, we have shown that the THz radiation can be concentrated to the $\sim 100 \text{ nm}$ transverse size in adiabatically graded plasmonic (metal/dielectric) waveguides. In the optimum adiabatically-graded, coaxial waveguide, which consists of the initial cone terminated with a funnel, the radiation of a 1 THz frequency whose wavelength is $300 \mu\text{m}$, can be compressed to a spot of 250 nm radius, where its intensity increases by a factor of $\times 250$. Even in the case of the extreme compression to a spot of the 100 nm radius, the THz intensity is enhanced by one order of magnitude with respect to the initial intensity of the $300 \mu\text{m}$ spot at the entrance of the waveguide. The physical process that limits the extent of this spatial concentration is the skin effect, i.e., penetration of the radiation into the metal that causes the losses: the THz field penetrates the depth of $l_s = 30 - 60 \text{ nm}$ of the metal, which by the order of magnitude determines the ultimate localization radius.

The THz nanoconcentration predicted in this Letter for optimally-graded adiabatic plasmonic waveguides provides unique opportunities for THz science and technology, of which we will mention below just a few. The nanoconcentration of the THz radiation will provide the THz ultramicroscopy with a THz source of unprecedented spatial resolution and brightness. The increase of the THz intensity by two orders of magnitude along with the novel high-power THz sources¹¹ would allow the observation of a wide range of electronic and vibrational nonlinear effects in metal, semiconductors, insulators, and molecules.

These nonlinear THz phenomena can be used to investigate behavior of various materials in ultrastrong fields, for nonlinear spectroscopy (including the multidimensional spectroscopy), and for monitoring and detection of various environmental, biological, and chemical objects and threats such as single bacterial spores and viruses. Such applications will certainly be helped by very large absorption cross sections of various materials in the THz region. A distinct and significant advantage of the adiabatic nanofocusing is that the THz energy is mostly con-

centrated in the hollow region of the waveguide, whose size can be made comparable with the size of the objects of interest: in the range from 1 micron to 70 nm, which is a typical range for bacteria and their spores, and viruses. This will assure high sensitivity and low background for the objects that are confined inside these waveguides.

Consider as a specific example the spectroscopy or detection of single particles, such as, e.g., anthrax spores, in the air. A sample containing the suspected nanoparticles in a gas, which can be air for the frequencies in the transparency windows, can be pumped through a THz waveguide, and the detection can be made for each particle in the gas separately on the basis of the two-dimensional nonlinear THz spectra that are expected to be highly informative for the detection and elimination of the false-positive alarms. Likewise, many other scientific, technological, environmental, and defense applications may become possible.

I. METHODS

A. Terahertz TM Wave in Finite-Conductivity Parallel Plate Waveguide

A parallel plate waveguide supports an even TM mode with wavenumber k , which satisfies the dispersion relation

$$\tanh\left(\frac{\kappa_d a}{2}\right) = -\frac{\varepsilon_d \kappa_m}{\varepsilon_m \kappa_d} \quad (5)$$

where $\kappa_d = (k^2 - \varepsilon_d k_0^2)^{1/2}$, $\kappa_m = (k^2 - \varepsilon_m k_0^2)^{1/2}$. In the terahertz range, ε_m is mainly imaginary, where $\text{Im } \varepsilon_m \gg 1$. Therefore, $\kappa_m \approx k_0 \sqrt{-\varepsilon_m} = l_s^{-1}(1 - i)$, where $l_s = 1/\text{Re } \kappa_m = \sqrt{2}/(k_0 \sqrt{|\varepsilon_m|})$ is the metal skin depth, which is on the order of tens of nanometers. We also assume that $\kappa_d a \ll 1$, which is always the case for the mode under consideration because either this mode is close to the TEM mode where $k = k_0 \varepsilon_d$, or the gap a is thin enough. This leads to a closed expression for the index of refraction of the mode, which is Eq. (2). Using this, one can check that $\kappa_d a \approx (\varepsilon_d a l_s / \lambda^2)^{1/2}$. Consequently, the applicability condition of the approximation used is

$$(\varepsilon_d a l_s / \lambda^2)^{1/2} \ll 1. \quad (6)$$

This condition is satisfied for the realistic parameters of the problem. For instance, for the frequency $f = 1$ THz, the skin depth for metals is $l_s \approx 60$ nm, while reduced wavelength is $\lambda = 75$ μm . The condition (6) is well satisfied for $a \ll 100$ μm , i.e., in the entire range of interest to us.

B. Terahertz TM Wave in Finite-Conductivity Coaxial Waveguide

Consider a coaxial waveguide (coax) with the inner wire radius r and the outer radius $R = r + a$, where a is

the dielectric gap width. The characteristic relation for the TM modes of this waveguide has the following form

$$\left(\frac{I_0(\kappa_d r)}{I_0(\kappa_m r)} - \xi \frac{I_1(\kappa_d r)}{I_1(\kappa_m r)}\right) \left(\frac{K_0(\kappa_d R)}{K_0(\kappa_m R)} - \xi \frac{K_1(\kappa_d R)}{K_1(\kappa_m R)}\right) = \quad (7)$$

$$\left(\frac{K_0(\kappa_d r)}{I_0(\kappa_m r)} + \xi \frac{K_1(\kappa_d r)}{I_1(\kappa_m r)}\right) \left(\frac{I_0(\kappa_d R)}{K_0(\kappa_m R)} + \xi \frac{I_1(\kappa_d R)}{K_1(\kappa_m R)}\right),$$

where $I_\nu(x)$ and $K_\nu(x)$ are modified Bessel functions, and $\xi = \frac{\varepsilon_d \kappa_m}{\varepsilon_m \kappa_d}$. This equation is quadratic with respect to ξ and can be written in the form $\alpha \xi^2 + \beta \xi + \gamma = 0$, where the coefficients α , β , and γ can be easily found by comparison to Eq. (7) as combinations of the Bessel functions. It can obviously be resolved for ξ yielding

$$\frac{\beta \pm \sqrt{\beta^2 - 4\alpha\gamma}}{2\alpha} = -\frac{\varepsilon_d \kappa_m}{\varepsilon_m \kappa_d}. \quad (8)$$

In the THz region, only the mode with the minus sign in Eq. (8) propagates. It can be treated in a manner similar to the mode described by Eq. (5). The equation (8) can be expanded over the small parameter $\kappa_d a \ll 1$, and the explicit form of the modal refraction index can be readily obtained as

$$n = \sqrt{\varepsilon_d} \left(1 + \left(\frac{I_0(\kappa_m r)}{I_1(\kappa_m r)} + \frac{K_0(\kappa_m R)}{K_1(\kappa_m R)}\right) \frac{l_s(1+i)}{2a}\right)^{1/2}, \quad (9)$$

where $\kappa_m = l_s^{-1}(1 - i)$. Similar to the wedge waveguide case, the applicability condition of this solution is given by Eq. (6).

C. WKB Solution for the TM Wave in Graded Waveguide

In the WKB approximation, a solution of the Maxwell equations can be represented as a wave with amplitude and phase that are slowly varying functions of y on the scale of local wavelength. The behavior in the transverse direction z is the same as for the non-graded system. The WKB solution is valid if the adiabatic parameter is small

$$\delta = \left|\frac{d}{dy} \frac{1}{k(y)}\right| \ll 1. \quad (10)$$

In the WKB approximation, the phase of the mode (eikonal) is given by an integral

$$\phi(y) = k_0 \int n(y) dy, \quad (11)$$

where $n(y)$ is the local refraction index of the mode. The behavior of wave amplitude as a function of the propagation coordinate y is found from the condition of flux conservation:

$$v_g(y) \int_{-\infty}^{\infty} W(y, z) dz = \text{const}, \quad (12)$$

where $v_g(y) = \partial\omega/\partial k$ is the wave local group velocity, and $W(y, z)$ is energy density in the mode.

This work was supported by grants from the Chemical Sciences, Biosciences and Geosciences Division of the Office of Basic Energy Sciences, Office of Science, U.S.

Department of Energy, a grant CHE-0507147 from NSF, and a grant from the US-Israel BSF. MIS is grateful to S. Gresillon for helpful remarks.

Correspondence and requests for materials should be addressed to MIS (email: mstockman@gsu.edu)

-
- ¹ L. Novotny and B. Hecht, *Principles of Nano-Optics* (Cambridge University Press, Cambridge, New York, 2006).
- ² M. I. Stockman, Phys. Rev. Lett. **93**, 137404 (2004).
- ³ E. Verhagen, L. Kuipers, and A. Polman, Nano Lett. **7**, 334 (2007).
- ⁴ C. Ropers, C. C. Neacsu, T. Elsaesser, M. Albrecht, M. B. Raschke, and C. Lienau, Nano Lett. **7**, 2784 (2007).
- ⁵ E. Verhagen, A. Polman, and L. Kuipers, Opt. Expr. **16**, 45 (2008).
- ⁶ L. Novotny and S. J. Stranick, Ann. Rev. Phys. Chem. **57**, 303 (2006).
- ⁷ A. Lewis, H. Taha, A. Strinkovski, A. Manevitch, A. Khatchatourians, R. Dekhter, and E. Ammann, Nature Biotechnology **21**, 1377 (2003).
- ⁸ J. Seelig, K. Leslie, A. Renn, S. Kuhn, V. Jacobsen, M. van de Corput, C. Wyman, and V. Sandoghdar, Nano Lett. **7**, 685 (2007).
- ⁹ F. D. Angelis, M. Patrini, G. Das, I. Maksymov, M. Galli, L. Businaro, L. C. Andreani, and E. D. Fabrizio, Nano Lett. p. DOI 10.1021/nl801112e (2008).
- ¹⁰ W. L. Chan, J. Deibel, and D. M. Mittleman, Rep. Prog. Phys. **70**, 1325 (2007).
- ¹¹ J. Hebling, K. L. Yeh, M. C. Hoffmann, and K. A. Nelson, IEEE Journal of Selected Topics in Quantum Electronics **14**, 345 (2008).
- ¹² H. T. Chen, R. Kersting, and G. C. Cho, Appl. Phys. Lett. **83**, 3009 (2003).
- ¹³ N. Klein, P. Lahl, U. Poppe, F. Kadlec, and P. Kuzel, J. Appl. Phys. **98**, 014910 (2005).
- ¹⁴ R. Lecaque, S. Gresillon, and C. Boccara, Opt. Expr. **16**, 4731 (2008).
- ¹⁵ M. A. Ordal, L. L. Long, R. J. Bell, S. E. Bell, R. R. Bell, J. R. W. Alexander, and C. A. Ward, Applied Optics **22**, 1099 (1983).
- ¹⁶ A. Sommerfeld, Ann. Phys. Chem. **67**, 233 (1899).
- ¹⁷ J. Zenneck, Ann. Phys. **23**, 846 (1907).
- ¹⁸ J. Saxler, J. Gómez Rivas, C. Janke, H. P. M. Pellemans, P. H. Bolivar, and H. Kurz, Phys. Rev. B **69**, 155427 (2004).
- ¹⁹ D. L. Mills and A. A. Maradudin, Phys. Rev. B **39**, 1569 (1989).
- ²⁰ J. B. Pendry, L. Martin-Moreno, and F. J. Garcia-Vidal, Science **305**, 847 (2004).
- ²¹ F. J. Garcia-Vidal, L. Martin-Moreno, and J. B. Pendry, Journal of Optics A: Pure and Applied Optics p. S97 (2005).
- ²² S. A. Maier, S. R. Andrews, L. Martin-Moreno, and F. J. Garcia-Vidal, Phys. Rev. Lett. **97**, 176805 (2006).
- ²³ F. Keilmann, Infrared Physics and Technology **36**, 217 (1995).
- ²⁴ A. Kramer, F. Keilmann, B. Knoll, and R. Guckenberger, Micron **27**, 413 (1996).
- ²⁵ F. Keilmann, D. W. vanderWeide, T. Eickelkamp, R. Merz, and D. Stockle, Opt. Commun. **129**, 15 (1996).
- ²⁶ Y. Shen, T. Watanabe, D. A. Arena, C. C. Kao, J. B. Murphy, T. Y. Tsang, X. J. Wang, and G. L. Carr, Phys. Rev. Lett. **99**, 043901 (2007).
- ²⁷ S. Komiyama, O. Astafiev, V. Antonov, T. Kutsuwa, and H. Hirai, Nature **403**, 405 (2000).
- ²⁸ B. Ferguson and X.-C. Zhang, Nature Materials **1**, 26 (2002).
- ²⁹ M. Tonouchi, Nature Photonics **1**, 97 (2007).
- ³⁰ D. Dragoman and M. Dragoman, Progress in Quantum Electronics **28**, 1 (2004).
- ³¹ K. V. Nerkararyan, A. A. Hakhoumian, and A. E. Babayan, Plasmonics **3**, 27 (2008).
- ³² F. Keilmann, J. Biol. Phys. **29**, 195 (2003).
- ³³ R. Merlin, Science **317**, 927 (2007).